Folding Angle Regulation by Curved Crease Design for Self-Assembling Origami Propellers

Shuhei Miyashita
Computer Science and Artificial Intelligence Laboratory
Massachusetts Institute of Technology
32 Vassar st. Cambridge, MA, 02139, USA
shuheim@csail.mit.edu

Isabella DiDio
Computer Science and Artificial Intelligence Laboratory
Massachusetts Institute of Technology
32 Vassar st. Cambridge, MA, 02139, USA
ididio@mit.edu

Ishwarya Ananthabhotla
Computer Science and Artificial Intelligence Laboratory
Massachusetts Institute of Technology
32 Vassar st. Cambridge, MA, 02139, USA
ishwarya@mit.edu

Byoungkwon An
Autodesk Research
Pier 9, San Francisco, CA, 94111, USA
kwon.an@autodesk.com

Cynthia Sung
Computer Science and Artificial Intelligence Laboratory
Massachusetts Institute of Technology
32 Vassar st. Cambridge, MA, 02139, USA
crsung@mit.edu

Slava Arabagi
Boston Children's Hospital
Harvard University
330 Longwood Avenue, Boston, MA, 02115, USA
badeaslava@gmail.com

Daniela Rus
Computer Science and Artificial Intelligence Laboratory
Massachusetts Institute of Technology
32 Vassar st. Cambridge, MA, 02139, USA
rus@csail.mit.edu

Abstract

This paper describes a method for manufacturing complex three dimensional curved structures by self-folding layered materials. Our main focus is to first show that the material can cope with curved crease self-folding and then to utilize the curvature to predict the folding angles. The self-folding process employs uniform heat to induce self-folding of the material and shows the successful generation of several types of propellers as a proof of concept. We further show the resulting device is functional by demonstrating its levitation in the presence of a magnetic field applied remotely.

1 Introduction

We are interested in developing rapid manufacturing of complex structures. To this end, we combine parameterized designs on origami pattern with planar fabrication into a new process for creating complex three dimensional shapes with curved surfaces by self-folding. In this paper we apply this fabrication method to manufacturing several types of propellers. We show experimentally that the propellers are functional units. While the results in this paper focus on propellers, they can be generalized to other complex shapes.

A rapidly increasing demand for manufacturing complex, iterative, or fine structures has drawn attention toward a fabrication technique that combines planar fabrication and origami-inspired transformations [1–3]. Recent innovations in origami technique [4, 5] have demonstrated that curved crease folding enables the generation of three dimensional geometries unachievable in traditional prismatic paper folding [4], which uses straight creases alone.

In the curved folding process, it is well known that folding also necessitates bending the sheet [4]. Various investigations have been conducted focusing on curved crease designs [6], rulings (see Section 3 for an explanation of rulings) [7, 8], sheet bending [9], formulation of the folding principle [10–12], or applications pertaining to car body design [13].

Self-folding is a recent technique aimed at rapid fabrication of objects by the folding of many small and complex creases [14–19]. To our knowledge, few approaches have attempted self-folding curved creases [20]. The engineering challenges here are (1) to precisely predict the folding angle of a curved crease, (2) to achieve self-folding of curved creases into a functional structure, and (3) to actuate the device after it has been self-folded, as a way of demonstrating functionality.

Under these presented challenges and goals, this paper contributes the following:

1. Simulations for estimating curved crease folding angles

2. An application of this algorithm toward designing propellers

3. An algorithm for computing self-folding crease patterns for objects with curved surfaces, such as propellers

4. A series of self-folding experiments for different propellers

5. Levitation experiments of the self-folded propellers by remotely applying a rotational magnetic field.

2 Outline

The methodology of curved crease self-folding described in this paper consists of the following steps. We model and derive a method for predicting a folding angle of a curved crease (Section 3). We outline the general guidelines for making an origami propeller (Section 4.1). We analyze the geometric relationship between the crease and folded propeller structure (Section 4.2). We develop an algorithm for automatically designing various types of origami propellers (Section 4.3). We build an electro-magnetic coil system with supporting electronics for remote actuation of the propeller (Appendix). We show the experimental results of self-folding curved creases (Section 5.1) and demonstrate self-folding of propellers with different crease curvatures (Section 5.2). We investigate the functionality of the folded propeller (Section 5.2). We conclude the study (Section 6).

3 Curved Crease Folding

This section investigates a basic theory of curved crease folding. We numerically analyze the relationship between shapes of various curvatures drawn on a two-dimensional crease pattern and the resulting three-dimensional folded shapes and curvature. Here, we employ the superellipse as an example of general curvature. A characteristic of the Superellipse is that it can represent a sector of major shapes such as squares, circles, or triangles, continuously being transformed by changing one parameter.

3

3.1 The Model

The curves we investigate are superellipses described on an x-y plane centered at $x = \frac{\pi}{2}$ with radius $\kappa = \frac{\pi}{2}$:

$$\left| \frac{x - \kappa}{\kappa} \right|^n + \left| \frac{y}{\kappa} \right|^n = 1. \tag{1}$$

The superellipse has a unique characteristic such that, by changing a single parameter, n, it changes curvature continuously from a square ($n \to \infty$) to a circle ($n = 2$), to a triangle ($n = 1$), and to a "star" ($n < 1$), while maintaining the width and the height (see Fig. 1 (a)). This is an ideal characteristic for our study since various curvatures can be compared in a single parametric space.

The positive half of the superellipse equation is

$$y = \kappa \cdot \left(1 - \left| \frac{x - \kappa}{\kappa} \right|^n \right)^{\frac{1}{n}}. \tag{2}$$

We depict the curves of $n = 1.5$, $n = 2$, and $n = 4$ in Fig. 1 (a), and show the illustration of the folded plane in Fig. 1 (b) with an example in the side picture.

The folding angle α is the angle between the two sides of the curve after it is folded, and whose change with respect to x can be described as [11]

$$
\begin{aligned}
\frac{d\alpha}{dx} &= \frac{\tan(\alpha(x))}{2 \cdot \frac{dx}{ds}} K_{2D}(x) \\
&\quad \cdot (\cot \beta_L(x) - \cot \beta_R(x)),
\end{aligned} \tag{3}
$$

where s is the arc length of the curve, which is a function of x:

$$s(x) = \int_0^x \sqrt{1 + \left(\frac{dy}{dx} \right)^2} \, dx, \tag{4}$$

K_{2D} is the curvature of the flat curve defined as

$$K_{2D} = \frac{\left| \frac{d^2 y}{dx^2} \right|}{\left(1 + (\frac{dy}{dx})^2 \right)^{\frac{3}{2}}}, \tag{5}$$

and $\beta_\cdot$ ($\cdot \in [R, L]$) is defined as the angle between the tangent line to the curve and the rulings of the surface that are made from the fold (Fig. 1 (b)).

Taking the derivative and reciprocal in Eq. (4) yields

$$\frac{dx}{ds} = \frac{1}{\frac{ds}{dx}} = \frac{1}{\sqrt{1 + \left(\frac{dy}{dx} \right)^2}}. \tag{6}$$

Rulings (or ruling lines) are straight lines that define a space curve by sweeping along the surface (shown as the red dot lines in Fig. 1 (b) and Fig. 8 (b)). Hypothesizing that both surfaces formed by the crease form cylindrical curvatures when folded into three dimension, $\beta_\cdot$ are calculated using vertical rulings (Fig. 1 (a)).

With vertical rulings, the angle β_R can be computed as

$$\beta_R = \tan^{-1} \left(\frac{1}{\frac{dy}{dx}} \right), \tag{7}$$

and β_L is simply

$$\beta_L = \pi - \tan^{-1} \left(\frac{1}{\frac{dy}{dx}} \right). \tag{8}$$

The derivative of the superellipse equation is

$$\frac{dy}{dx} = -\text{sgn} \left[\frac{x - \kappa}{y} \right] \cdot \left| \frac{x - \kappa}{y} \right|^{n-1}. \tag{9}$$

From Eq. (9) we obtain the second derivative of y as

$$
\begin{aligned}
\frac{d^2 y}{dx^2} &= (1 - n) \left| \frac{x - \kappa}{y} \right|^{n-2} \cdot \left(\frac{-x + \kappa}{y^2} \cdot \frac{dy}{dx} \right. \\
&\quad \left. + \frac{1}{y} \right) - \left| \frac{x - \kappa}{y} \right|^{n-1} \cdot 2\delta \left(\frac{x - \kappa}{y} \right),
\end{aligned} \tag{10}
$$

where δ is the Dirac delta function.

3.2 Simulation Results

Fig. 2 shows the simulation results of Eq. (3) for different surface conditions, which was run for n values of 1.5, 2, and 4. As the stiffness of the sheet material affects the bendable curvature of the surface and thus affects α, to run the simulation, we chose α at the end of the creases ($\alpha|_{\frac{dy}{dx} = 1}$; termed α_{end}) by supposing that the entire crease

consists of two straight lines divided from the middle of the curve to the edges (an example shown as the green line in Fig. 1 (a)). This way, when the surface is fully folded flat, $\alpha_{end} = \Gamma - \gamma$ (Γ and γ were obtained by taking the inverse tangent of the ratio of the horizontal and vertical radii of the curve), and when the surface folds up to $\pi/2$, $\alpha_{end} = (\Gamma - \gamma + \pi)/2$, premising that the actual value falls between them. This condition was selected by referring to our pre-tested manual folding experiments and the self-folding experiments appearing in the following sections.

The simulated result showed that the crease for $n = 4$ folded the most acutely while that for $n = 1.5$ folded the least in the middle of the creases (called α_{middle}) This trend is more clearly displayed in Fig. 3 with the change of folding angle α_{middle} with respect to n. The crease folded more as n increased, irrespective of α_{end}, although the tendency was more apparent for smaller values of α_{end}. This result suggests that when we plan to induce a difference in folding angles in real fabrication, it would be better to aim for smaller folding angles in order to achieve clear differentiation in their folding angles over different curved creases. We also verify this trend in later experiments (see Section 5.1).

Another noticeable trend is that α increased toward the center of the crease when $\alpha_{end} > \frac{\pi}{2}$, while it decreased when $\alpha_{end} < \frac{\pi}{2}$ This trend was observed with other conditions of α_{end} in the simulation, and is confirmed with manually folded models.

See the folding angles from experiments in Section 5.1.

4 Origami Propeller

This section builds further upon the established theoretical implications of curved crease folding to present the actual designs used in fabricating 3- and 4-blade propellers based on the origami designs introduced by Mitani [21] and the geometric rationale for having designed them in this manner. We first show a few largely well-known design guidelines on propeller design derived from the theories of aerodynamics. We then analyze the geometric relationship between a crease pattern and a three dimensional propeller so that the design parameters such as widths and lengths of blades can be dynamically optimized and reflected in the creases.

4.1 Design Guidelines

From helicopter aerodynamics, the thrust force, F_{th}, produced by a propeller consisting of multiple rotor blades is

$$\begin{aligned} F_{th} &= C_t \, \rho \, A \, \omega^2 \, r^2 \\ &\sim C_t \, \rho \, \omega^2 \, r^4, \end{aligned} \tag{11}$$

where A is the disk area swept by the blades, C_t is the aerodynamic thrust coefficient intrinsic to the blade profile, ω is the angular velocity, and r is the length of the blade [22]. The Reynolds number, Re, for the aerodynamic flow of a rotor in water is:

$$Re = \frac{c \, \omega \, r}{\nu}, \tag{12}$$

where c is the mean chord length of the blade (approximated at $1\,\mathrm{cm}$), ω is the angular velocity (approximated at $30\,\mathrm{Hz} \cdot 2\pi$), and ν is the kinematic viscosity. Approximating c as $1\,\mathrm{cm}$, $\omega \sim 30\,\mathrm{Hz} \cdot 2\pi$, $r \sim 1\,\mathrm{cm}$, and $\nu = 10^6\,\mathrm{m}^2/\mathrm{s}$, being the kinematic viscosity of water at $20°\mathrm{C}$, we obtain a $Re \sim 19000$. Given the high Re number and the fact that each blade of the rotor will be passing in the aerodynamic wake of the blade ahead of it (in hovering mode) the flow is expected to be turbulent. Thus a larger angle of attack of $45°$ for the rotor blades is chosen over the smaller pre-stall angles of attack to maximize the lift coefficient curve. Although increasing drag, this regime features a broader lift coefficient maxima thus allowing variability in angles of attack with little effect on lift.

Furthermore, the following facts on propeller engineering have been used as general design guidelines:

1. The lift force is proportional to the square of both angular velocity and disk radius swept by the blades, r, implying that scaling down of the disk area needs to be compensated by a proportional increase in rotational velocity, which greatly increases required power.

2. Longer blades provide larger lift forces at the expense of added weight.

3. A 45° angle of attack is chosen for each rotor blade per the above discussion.

4. A spanwise twist along the rotor blade that increases the angle of attack at the root and decreases it at the tip compensates for the increasing incoming stream velocity along the blade, thus allowing for a more uniform lift force profile [23]).

5. Increasing the number of blades mostly serves the purpose of reducing vibratory loads, since the power requirement increases proportionally with blade count.

4.2 Blade Geometry

The crease pattern of the 4-blade propeller is rotationally symmetric and is composed of four straight and four curved lines, as shown in Fig. 5(a). The center point is O, and a curved line has two sections: a curved section $\overparen{OI}$ and a straight section $\overline{IK}$. The curve can be one of many different types of a superellipse sector and does not have to intersect at position I. In this instance, a circular sector ($n = 2$) is used for the curve, and the angle of incidence is set to be $\angle IKJ$ 45°.

Fig. 5 (b) shows the folded propeller. Each of the corners A, B, C, D in Fig. 5(a) becomes an end A', B', C', D' of the blades in Fig. 5 (b), respectively. Each of the points E, F, G, H in Fig. 5(a),which represent the maximum amplitude of the circular sector curve, folds to the points E', F', G', H' of the blades in Fig. 5 (b), respectively.

Each point O, I, L in Fig. 5(a) is placed on point O', I', L' of the blades in Fig. 5 (b), respectively.

1. Blade Length. Let a denote the distance between O and I, b denote the distance between I and J, and t denote the shortest distance between F and $\overline{OI}$, where O' is the center point and $\angle OJB$ is 90°. In the folded propeller, the point I' is under the point O' at the center. Since $\angle IKJ$ is 45°, the length of $\overline{BK}$ is a and the length of $\overline{JK}$ is

b. The length of each blade is the equal to $\overline{BJ}$, which is $a + b$ (apothem).

2. Blade Width. The width of the blade is $t + b$ because the distance between E'' and center line ($\overline{I'L'}$) is t, and the distance between I' and $\overline{B'K'}$ is b, where E'' is the projected point of E' to the bottom (the plane of $\triangle I'L'B'$) and point K' is point K in folded status.

3. We look next at the outer circle formed by $\square E'F'G'H'$. Since $\overline{E'F'}$ of the folded propeller is $2t$, the radius of the outer circle is $\frac{2t}{\sqrt{2}}$.

The crease pattern of the 3-blade propeller is shown in Fig. 6(a). The design is similar to Fig. 5(a) in that all of the curvature lines are comprised of both a straight line and a curved line and they are pointed symmetrically toward the center O. As with the 4-blade propeller, each curved line is composed of two parts: a curved section $\overparen{OG}$ and a straight section $\overline{GI}$. The curve can be any line of the superellipse. We select 30° for the angle $\angle GIH$.

Fig. 6 (b) shows the folded 3-blade propeller seen from the top. Each corner A, B, C in Fig. 6(a) becomes each end A', B', C' of the blades in Fig. 6(b), respectively. Each point D, E, F in Fig. 6(a) is placed on each of the points D', E', F' of the blades in Fig. 6(b), respectively. Each point O, G, J in Fig. 6(a) is placed on each of the points O', G', J' of the blades in Fig. 6(b), respectively.

1. Blade Length. Let O denote the center point, and let $\angle OHB$ be 90°. Let a denote the distance between O and G, b denote the distance between G and H, and t denote the shortest distance between E and $\overline{OG}$. In the folded propeller, point E' and the correlating points on the other curved lines meet at the center. Since $\angle GIH$ is 30°, the length of $\overline{BI}$ is $\sqrt{3}a$ and the length of $\overline{IH}$ is $\sqrt{3}b$. The length of each blade is the equal to $\overline{BH}$ and is $\sqrt{3}(a + b)$.

2. Blade Width. If we project the propeller to the bottom, the angle between the projected

lines of $\overline{D'E'}$ and $\overline{G'O'}$ is $120°$. The width of the blade is $\frac{t}{\sqrt{3}} + b$ because the distance between E' and the center line is $\frac{t}{\sqrt{3}}$, and the distance between J and $\overline{CH}$ is b.

3. We look next at the outer circle formed by $\triangle D'E'F'$. Since $\overline{E'F'}$ of the folded propeller is $2t$, the radius of the outer circle is $\frac{2t}{\sqrt{3}}$.

4.3 Auto Generation of a Self-folding Crease Pattern and the Sheet

The fabrication of the propeller that was used in the study followed a protocol established previously by [16], used in [19], and is briefly outlined here. The developed self-folding sheet has a three layer structure, wherein a heat-sensitive contraction sheet is sandwiched between two rigid structural layers (Fig. 4). When heat is applied to the structure, the middle contraction layer shrinks. As a result, the entire structure folds in the direction that opens as a gap in the sheet.

We developed a Matlab program for auto-generation of multi-blade propeller crease patterns that allows users to vary the parameters of the design for the purpose of optimization. A graphic interface displays the front and back designs and allows users to adjust the gap widths along the folds (Fig. 7). A sample auto-generated pattern for a 4-blade propeller with circular curvature is shown in Fig. 7 (a). User-controlled parameters include: (1) the number of blades, (2) the type of curvature, either $n = 1.5, 2, 4$, or sinusoidal, (3) the apothem of the regular polygon, (4) the length of the curved crease, (5) the amplitude of the curved crease, (6) the incident angle of the curved crease, and (7) the gap width.

Finally, holes for the guiding pole, which was employed to stabilize the posture of a propeller during the levitation experiments, was added in each blade. When folding is complete, the hole appears as the conjugation of half-folded circles.

In the fabrication process, the generated crease pattern was printed onto a rigid sheet material using a laser cutter machine. After the excessive components of the pattern were removed, the construction sheet (polyvinylchloride; PVC) was placed between the front and the back forms of the crease pattern. These two layers were then laminated upon one another, sandwiching the contraction sheet. Lastly, the entire structure was subjected to uniform thermal application in a heated oven, thus self-folding from a two-dimensional crease pattern into a three dimensional propeller.

5 Results

This section presents the results from experiments on self-folding and on propeller levitation.

5.1 Single Curved Crease Self-folding

We fabricated three types of self-folding sheets of curved creases that we modeled in Section 3 and compared the folds to the simulated values of α. The self-folding experiments were performed on water in an oven (Cuisinart TOB-100) by setting the temperature to about $110°C$. The water was pre-warmed to approximately the deformation temperature of PVC ($\sim 50°C$) before the placement of a self-folding sheet. The sheets were folded on water to provide uniform heating (see [24]). In addition, folding on water helps reduce friction between the propeller and the ground. Under the set temperature of $110°C$, successful self-folding of the curved crease was observed (Fig. 8 (a)). Once folding started, the process maintained the speed of folding for a while before it slowed down and converged to the final angle.

The folded sheets are displayed in Fig. 8 (b). In our measurements, the folding angles at the middle (α_{middle}) are 2.0 rad ($113°$) for $n = 1.5$ crease, 1.9 rad ($107°$) for $n = 2$ crease, and 1.1 rad ($61°$) for $n = 4$ crease, showing that the most acutely folded crease was from $n = 4$ and the least folded from $n = 1.5$ (see the overlaid plots in Fig. 2). This trend was predicted in the simulation and also supports our intuition; when $n = 4$, the crease has almost a straight line in the middle. Approximating the curves as a straight crease should result in yielding a very small folding angle α. Conversely, when n

is smaller, $n = 1.5$, the crease can be approximated as two straight lines going from the edges intersecting in the middle. In this case, the folding angle reaches to $\frac{\pi}{2}$ given the surface can be folded fully flat.

The surface of the $n = 1.5$ curve induced the largest bend at the middle of the surface, whereas the $n = 4$ curve showed at the edge (compare the indications of ruling in Fig. 8 (b)). The influence of the stiffness of the self-folding sheet, which hindered the bending of the surface and was not counted in the model, can be recognized in the experimental results; with $n = 1.5$ and $n = 2.0$, the α_{middle} show smaller (more acute) values than expected by the model, whereas the influence can be seen on α_{end} with the $n = 4$ curve, in which smaller α_{end} was observed ($\alpha_{end} = 1.96$ rad (112°) for $n = 1.5$ crease, 1.76 rad (101°) for $n = 2$ crease, and 1.21 rad (70°) for $n = 4$ crease). This result implies a potential to improve the model by reflecting the stiffness of the material in rulings.

5.2   Propeller Self-Folding

We show the snapshots of self-folding with the $n = 2$ (circular) curve propeller design in Fig. 9.

Self-folding took about 3 minutes, from when deformation first began to when the sheet successfully achieved the targeted propeller shape. The self-folding successfully proceeded with 180° foldings along straight lines, resulting in about a 0.91 rad (52.2°) angle of attack (Fig. 10 (a)). In contrast, self-folded propellers of curved creases $n = 1.5$ showed a low attack angle of 0.86 rad (49.4°), while creases $n = 4$ showed a high attack angle of 1.08 rad (61.7°) (Fig. 10 (b)).

We further attempted two types of propeller self-foldings from the circular curve based on the crease designs in Fig. 7(b),(c). Fig. 11 shows the self-folded 3-blade propeller (on left) and 5-blade propeller (on right) for the verification that our parameterized design generates valid self-foldable propeller patterns. In the 3-blade model, compared to the 4-blade propeller, the number of blades are fewer and the length of the creases of straight lines is longer compared to the curved creases; thus, the design caused wider folding angles along the curved creases. The 5-blade model shows opposite attributes when folded. The folding angles of curved creases show smaller values compared to the 3-blade model. Currently, attaching paired magnets to odd number blade propellers is difficult for balancing propose, although we propose to utilize a diametrically magnetized hollow cylindrical magnet for future work.

5.3   Performance of the Propeller

To demonstrate its functionality as a self-folded structure, we levitated the self-folded 4-blade propeller inside water by remotely actuating it with a magnetic field. For this purpose, two pairs of two cylindrical magnets (axially magnetized, $\varnothing 3.27$ mm $\times H 1.62$ mm, K&J magnet) were horizontally attached onto the tip of two opposite blades pointing in the same directions (see Fig. 10 (b)). The two coupled magnets keep the positions on a blade by pinching it from both sides. To obtain a rotational magnetic field along the horizontal direction, we powered two-paired coil sets switching alternatively, accelerating the rotational speed of the magnetic field from 20 Hz to around 40 Hz (see Fig. 12 in Appendix: Remote Magnetic Actuation). Fig. 12(b) shows the height of levitation over time. The average heights of levitation for 15 s were 11.77 mm for $n = 1.5$, 14.69 mm for $n = 2$, and 13.02 mm for $n = 4$, which corresponds to 1.01, 1.26, and 1.11 body lengths, respectively, showing that the $n = 2$ propeller shows the best levitation level. While in motion, the propeller iteratively experienced levitation and step out resulting from the levitation, changing the height repeatedly. Step out occurred as the propeller moved afar from the coils by levitation and thus received a weaker magnetic field.

A unique behavior was from the propeller of $n = 1.5$, where levitation proceeded slowly compared to the other propellers due to the shallower angle of attack. As a result, it showed a rather long duration for levitation before stepping out, appearing in the smooth trajectory in the figure. Despite the environment being underwater, the experiment shows the functional motion as

a propeller, which was generated by self-folding from a sheet structure.

6 Conclusion

This study shows a method of rapid prototyping of 3D curved structures based on a self-folding technique. We explore design and modeling approaches for regulating folding angles by changing the curvature of creases and applied this to the fabrication of propeller blades. Our results demonstrating self-folding propellers supported by mathematical estimation, automated crease generation, and self-folding materials shows promise for the automation of fabricating complex three dimensional structures through a folding process of layered intelligent sheet materials.

Acknowledgment

Appendix: Remote Magnetic Actuation

A setup consisting of four electromagnetic solenoid coils was employed to apply a rotational magnetic field to the propeller. The magnetic coils consist of copper wire wound on square pillar-shaped ferrous cores of cross-sectional side lengths $2D$. An xyz coordinate set is defined for each coil, such that the origin lies at the centroid of each coil, the $x - y$ plane is parallel to the surface of the coil, and z is normal to the surface, as illustrated in Fig. 13. A small magnet a distance from the coil can be regarded as a magnetic dipole moment $\boldsymbol{m}$. Assuming that the magnet's shape can be approximated as a spherical shape of radius a, $\boldsymbol{m}$ can be described with the saturation magnetization $\boldsymbol{M}_{sat}$ as

$$\boldsymbol{m} = \frac{4}{3}\pi a^3 \boldsymbol{M}_{sat}, \tag{13}$$

where M_{sat} is intrinsically given by the material of the magnet.

The z-directed magnetic flux density B_z centered on the z axis at position z is

$$B_z = \frac{\mu_0 I}{4\pi} \frac{2D^2}{(D^2 + z^2)^{\frac{3}{2}}}. \tag{14}$$

The gradient along the z axis is then

$$-\frac{\partial B_z}{\partial z} \propto \frac{2z}{(D^2 + z^2)^{\frac{5}{2}}}. \tag{15}$$

When $D \ll z$, using Taylor series, the force that the magnet experiences is proportional to

$$-\frac{\partial B_z}{\partial z} \sim \frac{2z}{\left(1 + \frac{5}{2D^2}z^2\right)}. \tag{16}$$

The four coils were evenly spaced around the central vertical axis and tilted at $45°$ from the horizontal. The stage was set on the point where the z axes of all the coils intersect. This configuration allows the generation of any arbitrary magnetic field vector at the stage via the superposition of individual fields of each coil (see Fig. 13). In addition, a quasi-uniform field is guaranteed with arbitrary strength along the $^Gx - {}^Gy$ plane and a non-uniform field along the ^Gz-direction. Because the magnetic field strength is stronger at positions closer to the coils, the propeller can experience magnetic step out as it levitates higher and enters a relatively weaker magnetic field region.

The force $\boldsymbol{F}$ and the torque $\boldsymbol{\tau}$ that the magnet experiences in a magnetic flux density $\boldsymbol{B}$ are given as

$$\boldsymbol{F} = (\boldsymbol{m} \cdot \nabla)\boldsymbol{B}, \tag{17}$$
$$\boldsymbol{\tau} = \boldsymbol{m} \times \boldsymbol{B}, \tag{18}$$

where $\boldsymbol{B}$ is the globally created superimposed magnetic flux density of four coils. The torque reaches the maximum when the relative angle between the magnet and the applied field reaches $90°$.

In real measurements, the coil exerted magnetic fields of $7.0\,\mathrm{mT}$, $5.7\,\mathrm{mT}$, and $19.7\,\mathrm{mT}$ at a current flow of $4\,\mathrm{A}$ measured at the center of the surface at respective distances of $z = 0\,\mathrm{mm}$ (on the surface), $z = 10\,\mathrm{mm}$, and $z = 40\,\mathrm{mm}$. The amount and duration of the current to the coils were driven by motordrivers (SyRen10), which were manually controlled through serial communication with a PC via ArduinoMega.

References

[1] Whitney JP, Sreetharan PS, Ma K, Wood RJ. 2011, Pop-up book MEMS. Journal of Micromechanics and Microengineering. 21(11):115021.

[2] Hoover AM, Steltz E, Fearing RS. 2008, RoACH: An autonomous 2.4g crawling hexapod robot. In: IEEE/RSJ International Conference on Intelligent Robots and Systems (IROS). pp. 26–33.

[3] Felton S, Lee DY, Cho KJ, Wood RJ. 2014, A Passive, Origami-Inspired, Continuously Variable Transmission. In: IEEE International Conference on Robotics and Automation. Hong Kong. pp. 2913–2918.

[4] Demaine ED, Demaine ML, Koschitz D, Tachi T. 2011, Curved Crease Folding: a Review on Art, Design and Mathematics. In: Proceedings of the IABSE-IASS Symposium: Taller, Longer, Lighter (IABSE-IASS 2011). London, England.

[5] Koschitz D, Demaine ED, Demaine ML. 2008, Curved Crease Origami. In: Abstracts from Advances in Architectural Geometry (AAG 2008). Vienna, Austria. pp. 29–32.

[6] Huffman DA. 1976, Curvature and creases: A primer on paper. Computers, IEEE Transactions on. 100(10):1010–1019.

[7] Duncan JP, Duncan J. 1982, Folded developables. Proceedings of the Royal Society of London A Mathematical and Physical Sciences. 383(1784):191–205.

[8] Fuchs D, Tabachnikov S. 1999, More on paper folding. The American Mathematical Monthly. 106(1):27–35.

[9] Kergosien YL, Gotoda H, Kunii TL. 1994, Bending and Creasing Virtual Paper. IEEE Computer & Applications. 14:40–48.

[10] Dias MA, Santangelo CD. 2012, The shape and mechanics of curved-fold origami structures. Europhysics Letters. 100:54005–p1 – 54005–p6.

[11] Tachi T. 2013 Composite Rigid-Foldable Curved Origami Structure. In: The First Conference Transformables, School of Architecture. Seville Spain.

[12] Yao Z, Bowick M, Ma X, Sknepnek R. 2013, Planar sheets meet negative-curvature liquid interfaces. Europhysics Letters. 101(4):44007.

[13] Kilian M, Flöry S, Chen Z, Mitra NJ, Sheffer A, Pottmann H. 2008, Curved Folding. ACM Transactions on Graphics. 27(3):#75, 1–9.

[14] Hawkes E, An B, Benbernou NM, Tanaka H, Kim S, Demaine ED, et al. 2010, Programmable matter by folding. Proceedings of the National Academy of Sciences. 107(28):12441–12445.

[15] Felton SM, Tolley MT, Shin B, Onal CD, Demaine ED, Rus D, et al. 2013, Self-folding with shape memory composites. Soft Matter. 9:7688–7694.

[16] Miyashita S, Onal CD, Rus D. 2013, Self-pop-up Cylindrical Structure by Global Heating. In: IEEE/RSJ International Conference on Intelligent Robots and Systems (IROS), pp. 4065–4071.

[17] Yasu K, Inami M. 2012, POPAPY: instant paper craft made up in a microwave oven. In the 9th International Conference on Advances in Computer Entertainment.

[18] Tolley MT, Felton SM, Miyashita S, Aukes D, Rus D, Wood RJ. Self-folding origami: shape memory composites activated by uniform heating. The IOP Journal Smart Materials and Structures. doi:10.1088/0964-1726/23/9/094006.

[19] Miyashita S, Meeker L, Göldi M, Kawahara Y, Rus D. 2014, Self-Folding Printable Elastic Electric Devices: Resistor, Capacitor, and Inductor. In: IEEE International Conference on Robotics and Automation (ICRA), pp. 1446–1453.

[20] Guberan C, 2012, Available from: `http://vimeo.com/39914902`.

[21] Mitani J. 2009, Fushigina Kyutai Rittai Origami Tokyo: Futami shobo.

[22] Leishman JG, editor. 2006, Principles of Helicopter Aerodynamics. Cambridge University Press, 2nd ed.

[23] Keys C, Tarzanin F, McHugh F. 1987, Effect of Twist on Helicopter Performance and Vibratory Loads. In 13th European rotorcraft forum.

[24] Miyashita S, Meeker L, Göldi M, Tolley MT, Wood RJ, Rus D. Self-Folding Miniature Elastic Electric Device. The IOP Journal Smart Materials and Structures. doi:10.1088/0964-1726/23/9/094005.
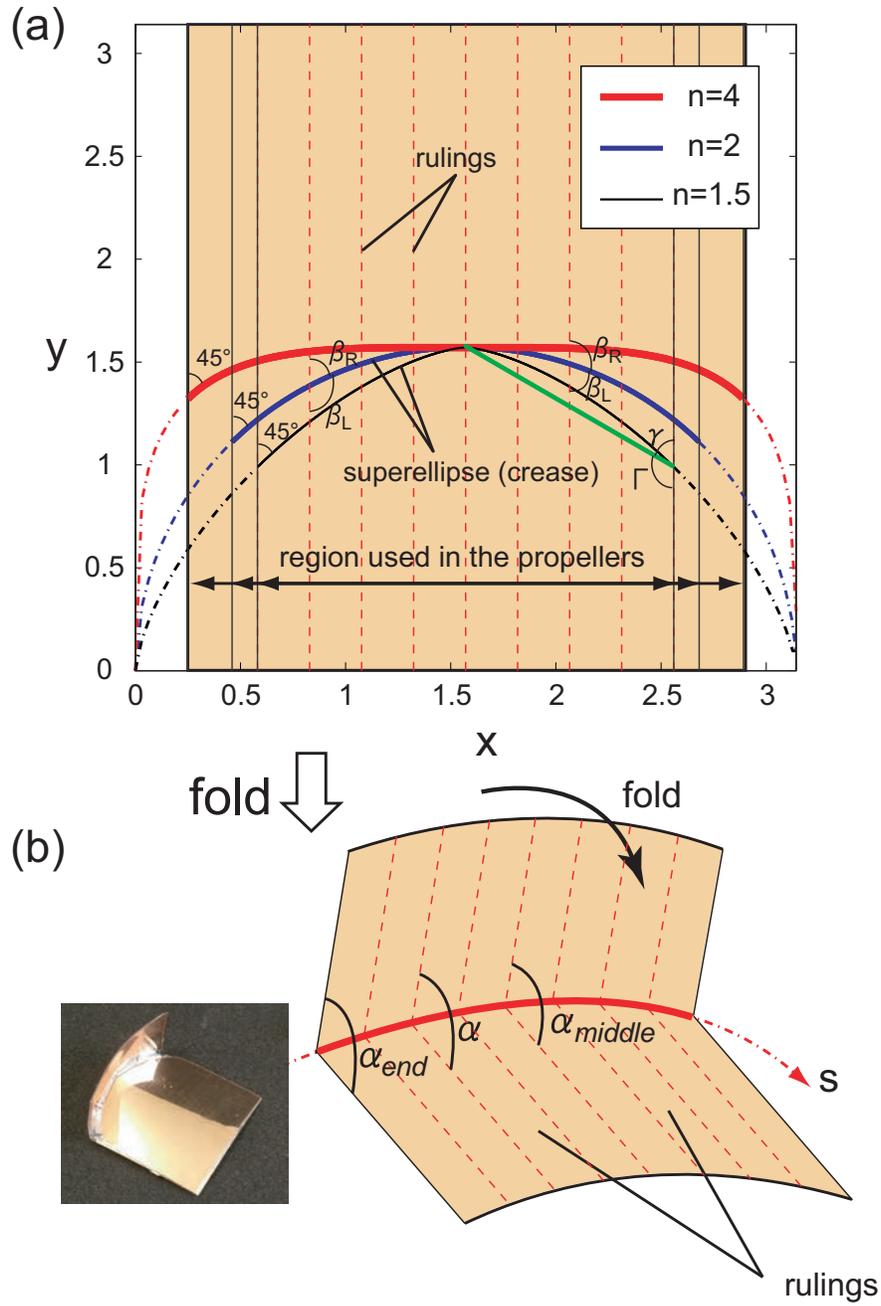
Figure 1: Curved crease folding. (a) Superellipse curves of $n = 1.5$, $n = 2$, and $n = 4$. The rulings and corresponding β. are defined. (b) The folding angle α over arc lengths s.
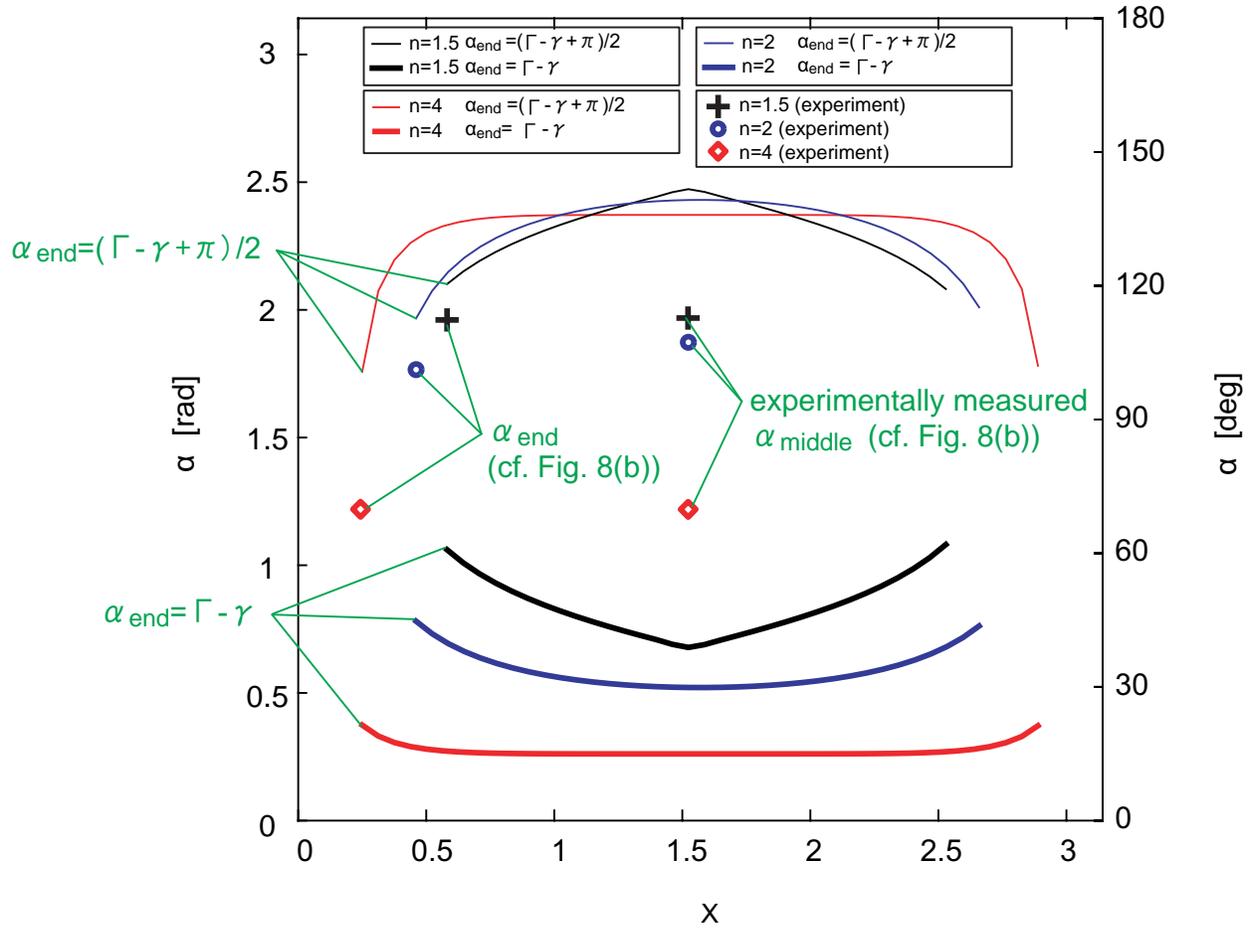
Figure 2: Simulated folding angles α, for $n = 1.5, 2,$ and 4, with different conditions of α_{end}. Experimental results of α_{end} and α_{middle} are superimposed.
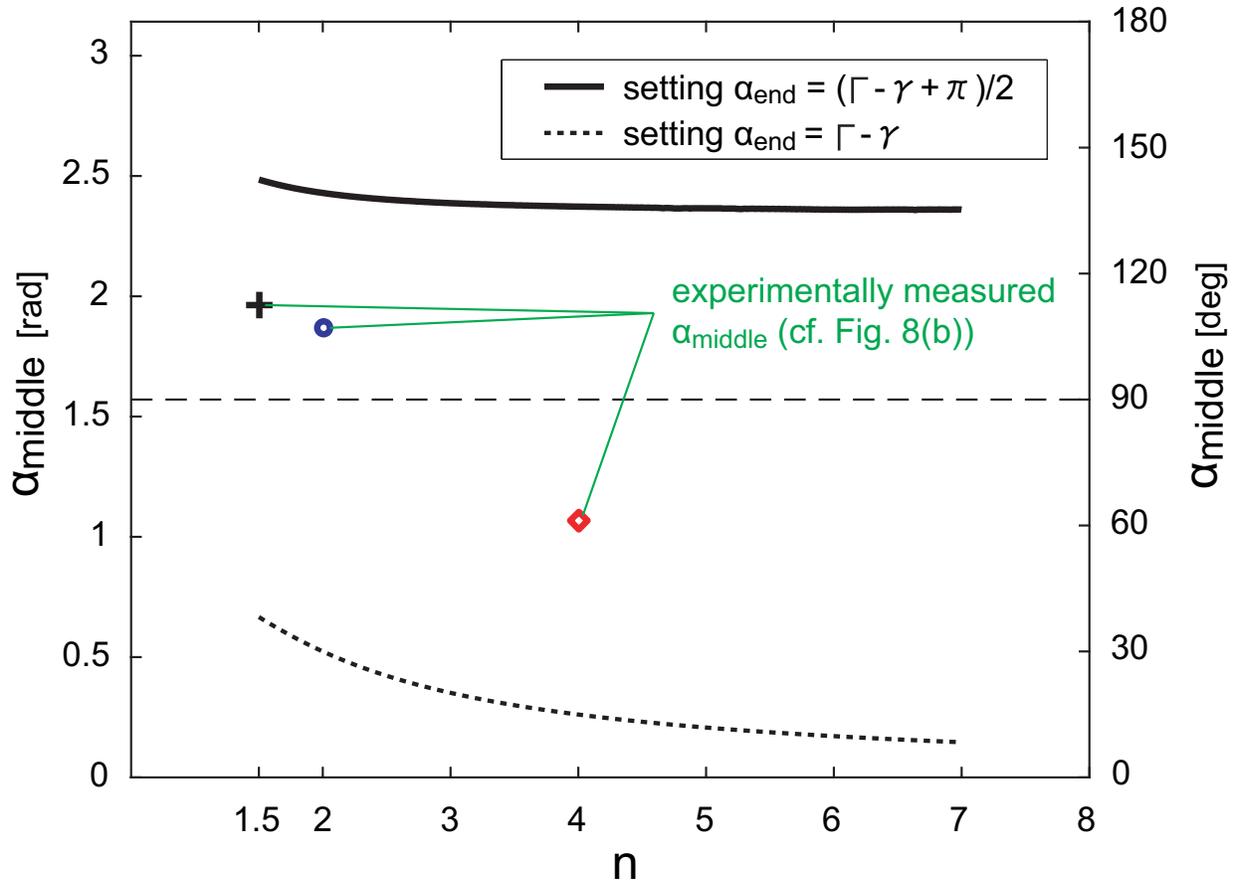
Figure 3: Change of α_{middle} over n for $\alpha_{end} = (\Gamma - \gamma + \pi)/2$ (upper curve) and $\alpha_{end} = \Gamma - \gamma$ (lower curve). As a general trend, the larger n becomes, the more acutely it folds.

structural layer
(top and bottom)

gap (crease)

front

back

contraction layer
(PVC; middle)

slit

heat

α
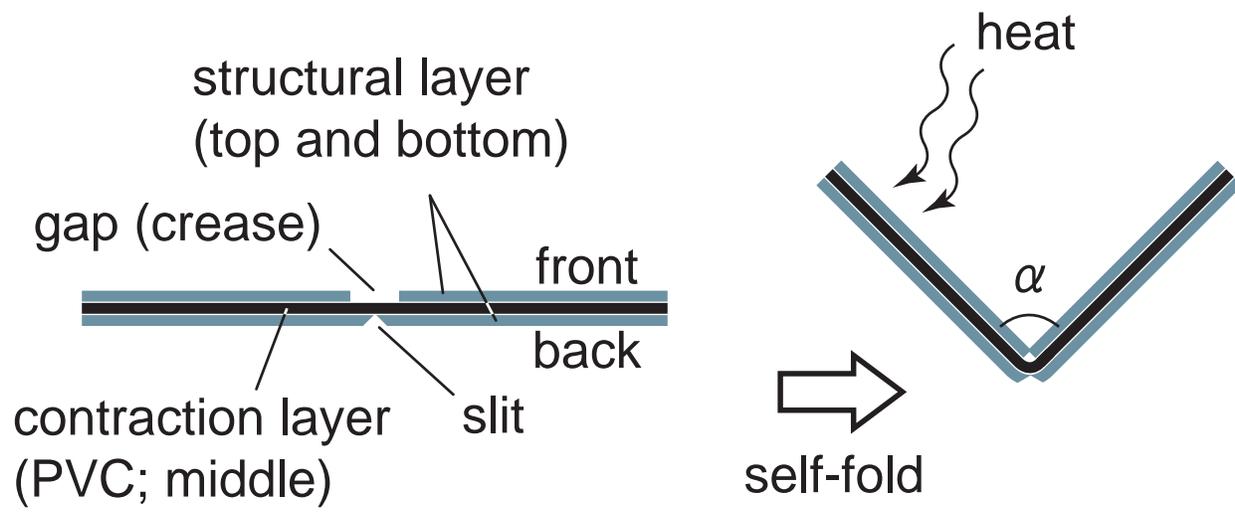
self-fold

Figure 4: Three layer structure for the heat sensitive self-folding method [16].
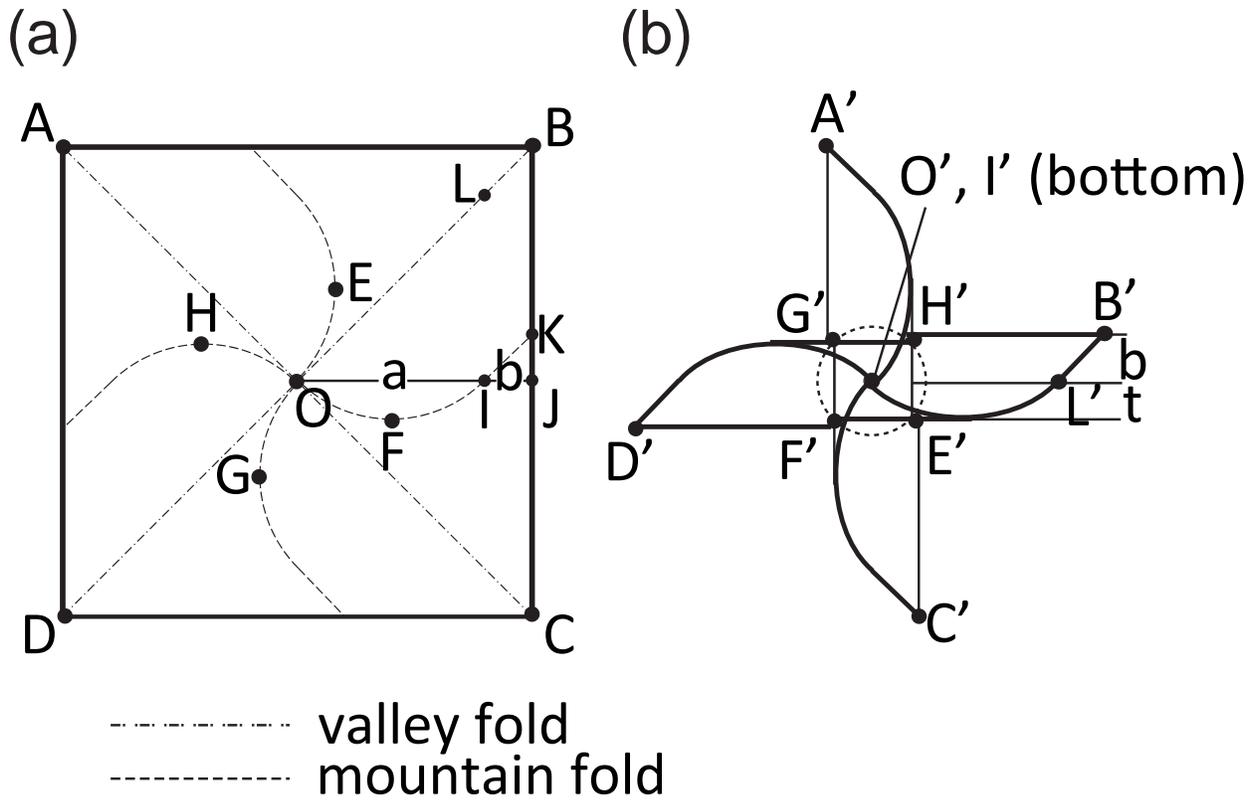
Figure 5: 4-blade origami propeller. (a) The crease pattern. (b) Folded propeller in top view.

(a)

B

D

I

A a b

F O t G H

E

J

C

valley fold
mountain fold

(b)

B'

F'

D'

A'

E'

O', G'
(bottom)

J' C'

b
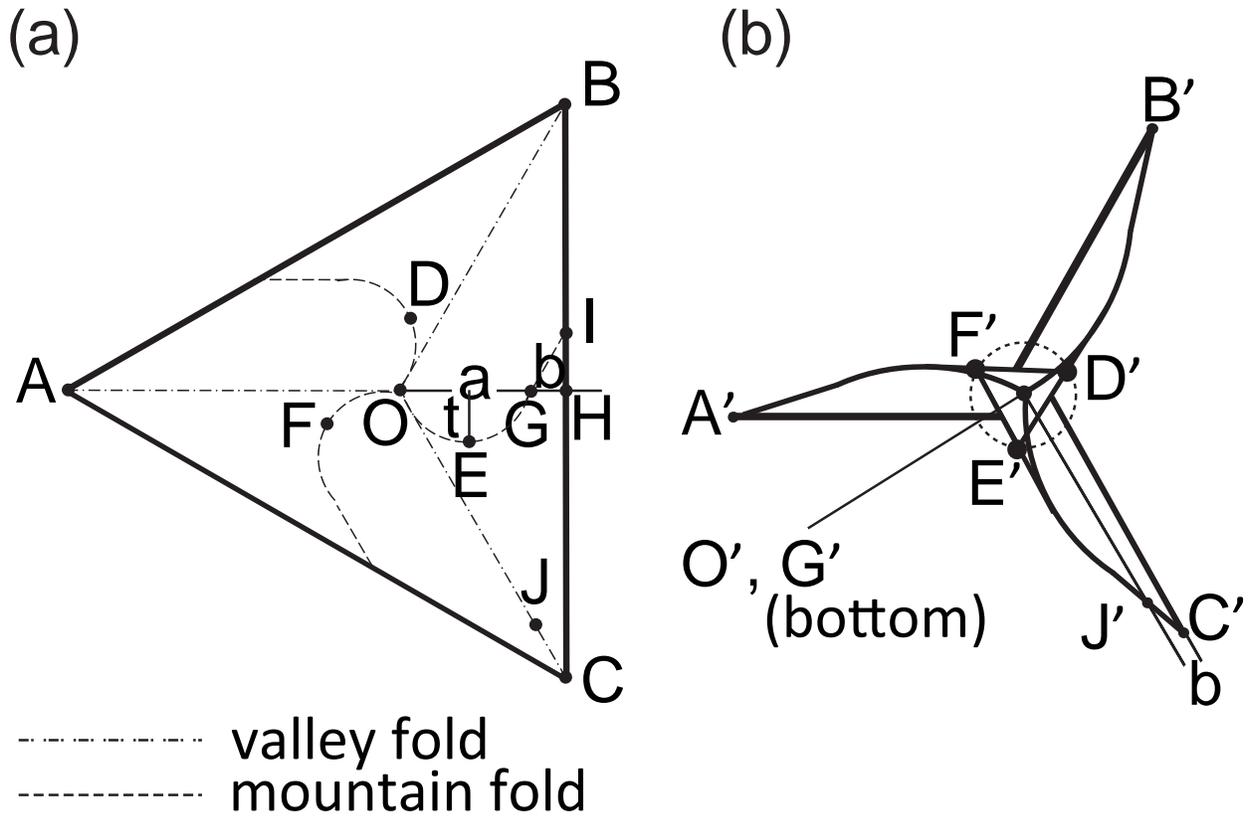
Figure 6: 3-blade origami propeller. (a) The crease pattern. (b) Folded propeller in top view.
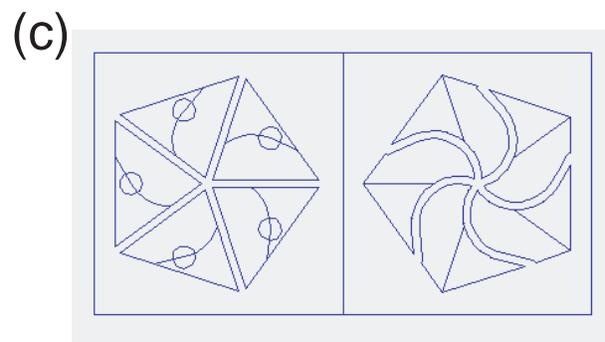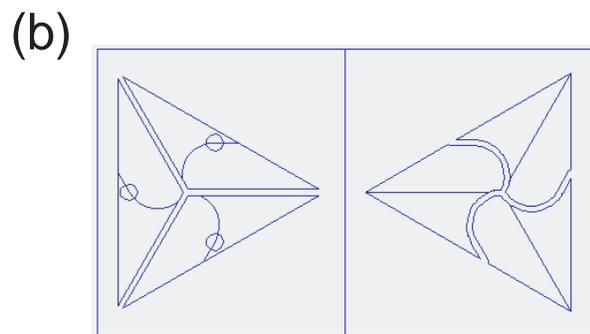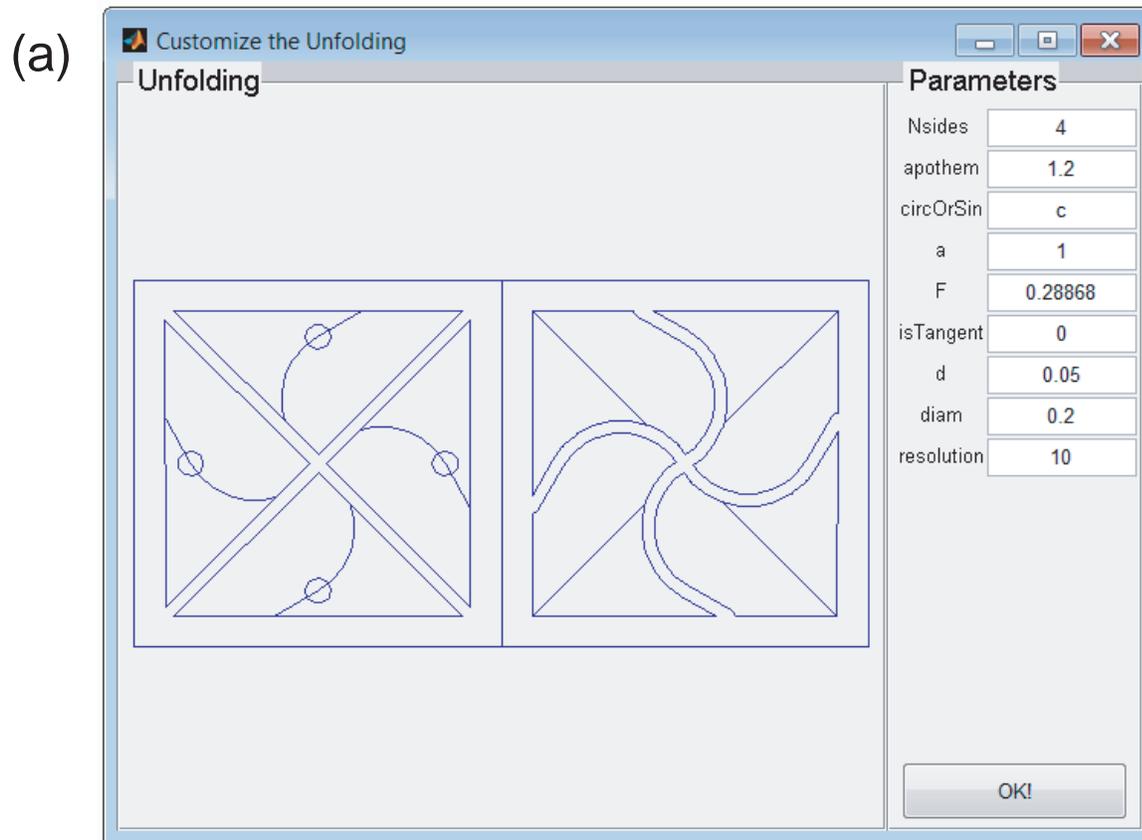
Figure 7: Automated self-folding crease pattern generation. (a) The user interface. (b) Front and back crease pattern of a 3-blade propeller. (c) Crease pattern of a 5-blade propeller. In a curved crease, a superellipse and a straight line are connected smoothly at an inclination of 45°.
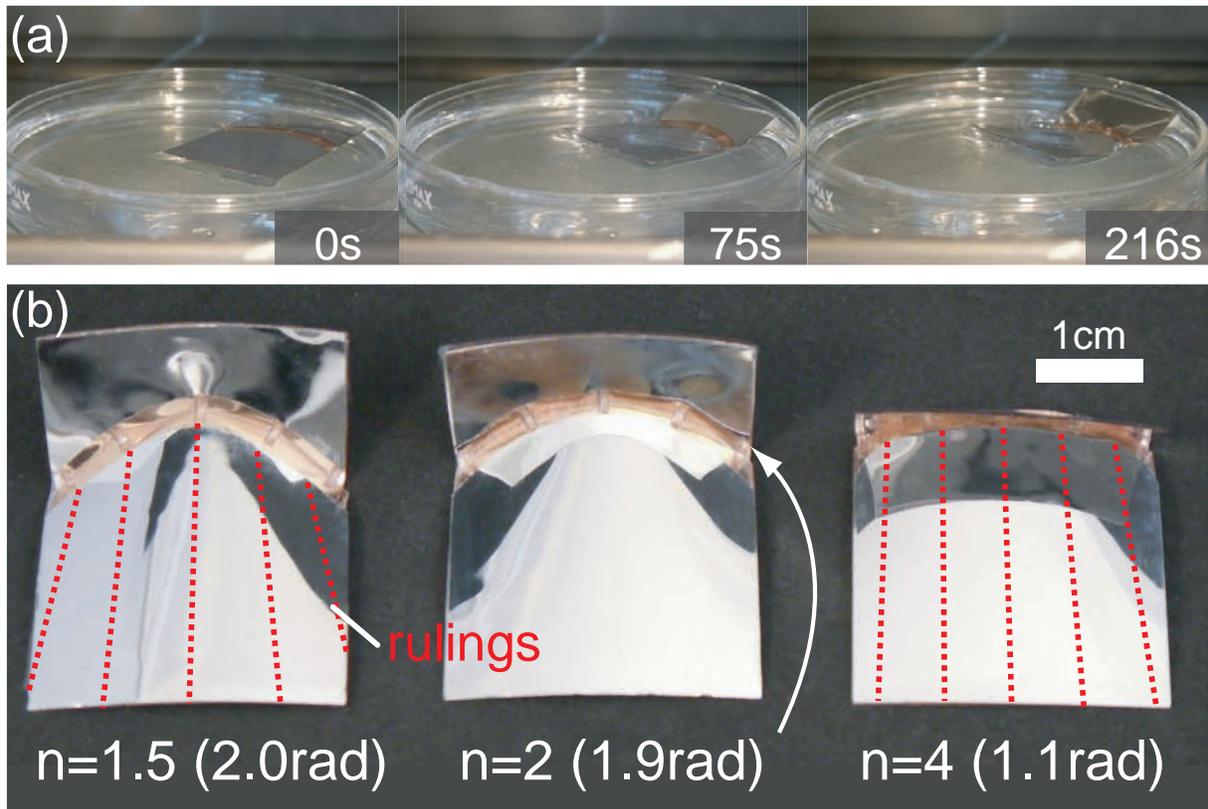
Figure 8: Self-folded curved creases with different curvature patterns. (a) The snapshots of the $n = 2$ model while self-folding. (b) Self-folded curved creases ($n = 1.5, 2, 4$ from left to right, respectively).
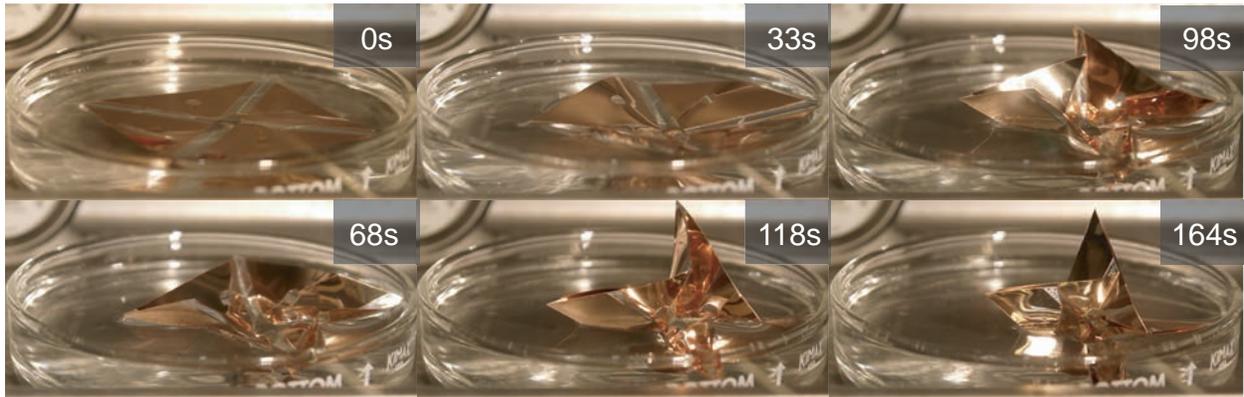
Figure 9: Self-folding 4-blade propellers ($n = 2$ model). The whole process was completed in about 3 minutes.
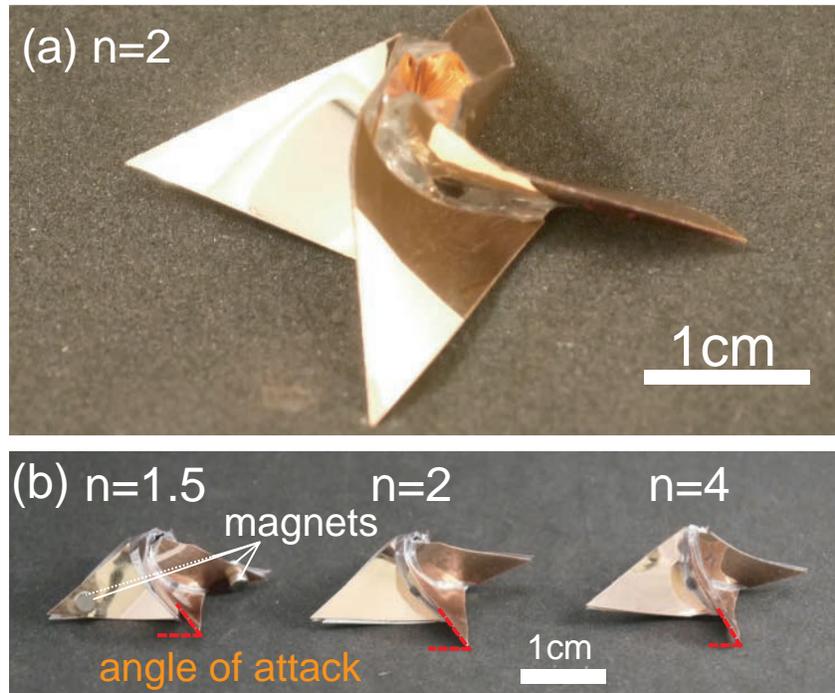
Figure 10: Self-folded 4-blade propellers. (a) The angled view. (b) Comparison of angle of attack of $n = 1.5$, $n = 2$, and $n = 4$ propellers.
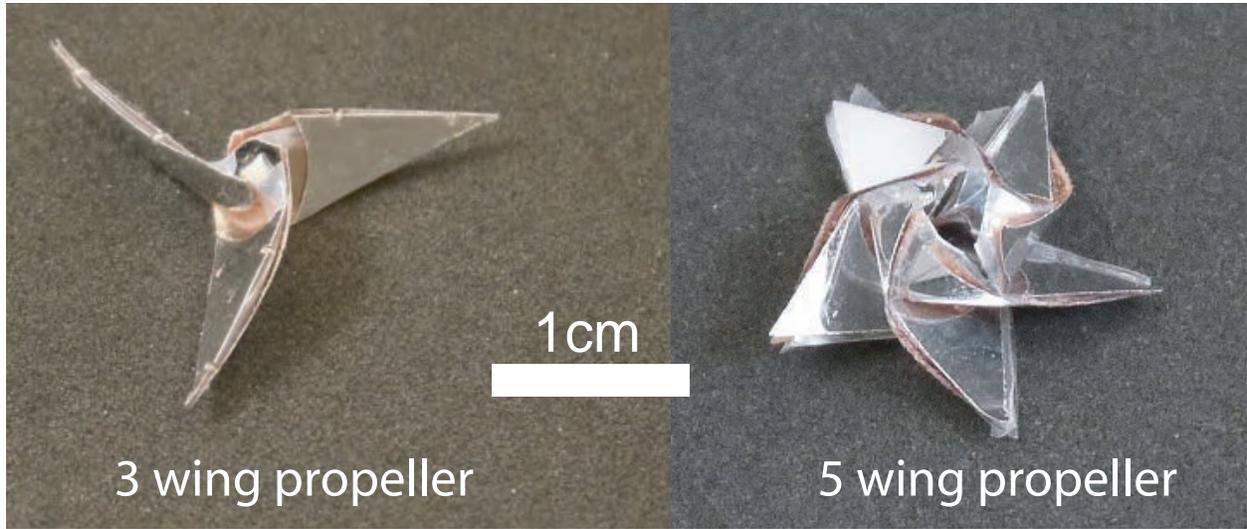
3 wing propeller   1cm   5 wing propeller

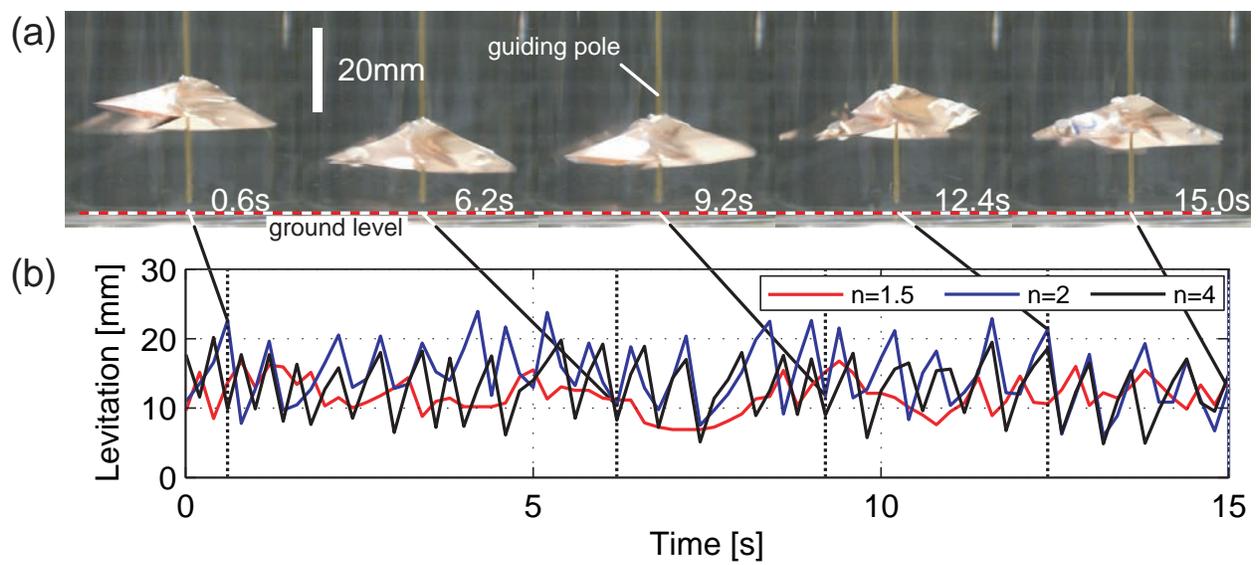Figure 11: Self-folded 3-blade propeller (left) and 5-blade propeller (right).

Figure 12: Attained levitation of origami propellers. (a) Snapshots of levitation from $n = 2$ propeller, (b) Height of levitation over time.

pole

propeller

${}^{G}z$

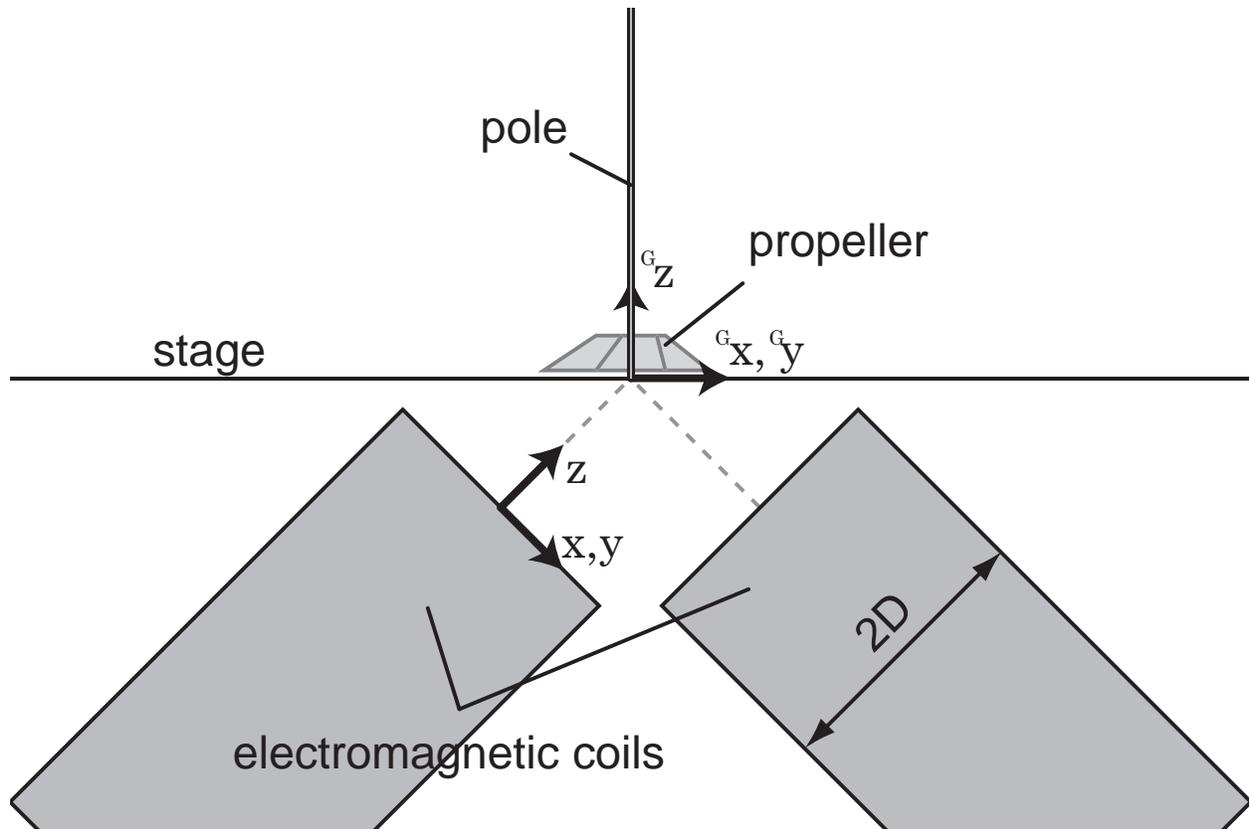stage

${}^{G}x$, ${}^{G}y$

z

x,y

2D

electromagnetic coils

Figure 13: The developed electromagnetic coil system.